Title: Inertio-elastic focusing of bioparticles in microchannels at ultra-high throughput

Authors: Eugene J. Lim[1,2]†, Thomas J. Ober[3]†, Jon F. Edd[2], Salil P. Desai[2], Douglas Neal[4], Ki Wan Bong[2], Patrick S. Doyle[5], Gareth H. McKinley[3*] & Mehmet Toner[2*]

Affiliations:
[1]Electrical Engineering and Computer Science Department, Massachusetts Institute of Technology, Cambridge, MA 02139
[2]Center for Engineering in Medicine and Surgical Services, Massachusetts General Hospital, Harvard Medical School, Boston, MA 02129
[3]Mechanical Engineering Department, Massachusetts Institute of Technology, Cambridge, MA 02139
[4]LaVision Inc., Ypsilanti, MI 48197
[5]Chemical Engineering Department, Massachusetts Institute of Technology, Cambridge, MA 02139
†These authors contributed equally to this paper.
*Correspondence to: gareth@mit.edu, mehmet_toner@hms.harvard.edu

Abstract:

We report on a hydrodynamic approach that enables deterministic focusing of beads, mammalian cells, and anisotropic hydrogel particles in a microchannel at extremely high flow rates. We show that upon addition of micromolar concentrations of hyaluronic acid (HA), the resulting fluid viscoelasticity can be used to control the focal position of bioparticles at Reynolds numbers up to $Re \approx 10{,}000$ with corresponding flow rates and particle velocities up to 50 $ml.min^{-1}$ and 130 $m.s^{-1}$, respectively. We also find that controlled manipulation of cell-sized particles in water in the absence of HA is not possible at Reynolds numbers beyond 2500±500 due to the onset of inertial turbulence. We demonstrate that it is not secondary flows or shear-thinning in the fluid rheology but the presence of viscoelastic normal stresses that drive the deterministic particle migration in the HA solution. This study explores a previously unattained regime of inertio-elastic fluid flow and demonstrates bioparticle focusing at flow rates that are the highest yet achieved.

One Sentence Summary:

We demonstrate inertio-elastic focusing of rigid beads, deformable cells, and anisotropic PEG particles using a viscoelastic biopolymer additive at Reynolds numbers up to 10,000.

Main Text:

The ability to continuously manipulate and separate particles or cells from very large volumes of fluids at high throughput is critical for many biomedical, environmental and industrial applications (*1*, *2*). Although microfluidic technologies such as immunoaffinity capture (*3*), deterministic lateral displacement (*4*), and microporous filtration (*5*) have revolutionized the sorting of cells from bodily fluids, they have typically been limited to low throughput. More recently, directed inertial focusing of particles towards specific fluid streamlines in straight (*6*, *7*) and curved (*8*, *9*) microchannels in Newtonian fluids (of density ρ and viscosity μ) has been observed at moderate Reynolds numbers ($Re = \rho UH/\mu \approx 100$), where U is the particle velocity and H is the channel cross-sectional dimension. However, the upper bound of sample throughput for inertial focusing in microchannels is likely limited by the hydrodynamic transition from laminar flow to turbulent flow and has not been characterized for $Re > 1500$ (*10*). In separate studies, particle migration due to elastic effects has also been explored (*11*, *12*, *13*) using particles suspended in viscoelastic fluids at moderate to high Weissenberg numbers (*14*) ($Wi = \lambda U/H$, where λ is the characteristic relaxation time), but here viscoelastic focusing was limited to only moderate Reynolds numbers ($Re < 10$). When simultaneously important, inertia and elasticity can act constructively to stabilize a given flow (*15*, *16*), but it is unknown whether viscoelastic flows at high Reynolds number ($Re > 2000$) can facilitate inertio-elastic particle migration in microchannels. There are significant technical challenges to studying particle focusing at very high Reynolds numbers. One challenge is building microfluidic devices that can withstand pressure drops that may easily approach 5000 PSI (3.4×10^7 Pa) depending on channel dimensions and operating flow rate. Another challenge is tracking individual particles with particle velocities that can easily exceed 100 m/s.

Here, we used an epoxy-based fabrication technique (Fig. S1) to construct a 35-mm long straight channel with $H = 80 \pm 5$ μm square cross-section capable of achieving a maximum throughput of $Q = 50$ ml.min^{-1} ($Re = 10{,}400$, $U = 130$ m.s^{-1}). We infused test fluids into the microchannel using a high-pressure (10,000 PSI), high-throughput (50 ml.min^{-1}) syringe pump. Long-exposure fluorescence (LEF) imaging was used to efficiently detect particle migration based on aggregate signal intensity (Fig. 1A). Particle trajectory analysis (PTA) (*17*) was used to observe specific features (*e.g.*, 3D position, orientation, deformation) of the particle migration based on individual particle statistics. Micro particle imaging velocimetry (μ-PIV) was used to measure the local fluid velocity in the microchannel (based on 1-μm polystyrene beads), while particle tracking velocimetry (PTV) was used to measure discrete particle velocities in the microchannel (based on 8-μm polystyrene beads).

To study particle migration in viscoelastic flows at high Reynolds number, we selected hyaluronic acid (HA) as a model viscoelastic additive based on its biocompatibility and the turbulent drag-reducing properties that have been documented in the flow of blood (*18*) and synovial fluid (*19*). The Reynolds number was calculated based on a shear-rate dependent viscosity as defined by the Carreau model (see Supplementary Materials). This viscosity is evaluated at the relevant wall shear rate in the fluid $\dot{\gamma} = 9.4U/H$, based on the analytical solution for the velocity field of a Newtonian liquid in a square channel (with cross-sectional dimension H). The Weissenberg number was calculated based on a fluid relaxation time $\lambda = 8.7 \times 10^{-4}$ s measured experimentally using the thinning dynamics of a liquid filament (*20*). The measured pressure drop ΔP over the entire fluidic network was measured by the syringe pump for a given

imposed flow rate Q (Fig. 1B). For water, ΔP_{water} first increased linearly with Q before increasing more rapidly at $Re \approx 2500 \pm 500$, which indicated a transition to turbulence. In the HA solution, ΔP_{HA} scaled sublinearly with Q due to shear-thinning effects, and $\Delta P_{HA} > \Delta P_{water}$ (due to the higher fluid viscosity) for $Q < Q_t$, where $Q_t \approx 12 \pm 2.5$ ml.min^{-1} is the flow rate at which the flow of water transitioned from laminar to turbulent. However, for flow rates $Q > Q_t$, ΔP_{HA} continued to scale sublinearly with Q (up to 50 ml.min^{-1}), which suggests that the flow of the HA solution remained laminar even up to $Re \approx 10{,}000$. Using a microfluidic rheometer we also measured the viscosity of the HA solution (M_w = 1650 kDa, 0.1% w/v) before and after sample processing within the range of shear rates explored in the microchannel ($10^3 < \dot{\gamma} < 10^7$ s^{-1}). The shear viscosities of the native and used samples were found to remain almost unchanged, indicating that shear-induced degradation of the sample (*21*) was not a major issue (Fig. S3).

With the ability to achieve laminar microchannel flow at Reynolds number up to $Re \approx 10{,}000$ in a viscoelastic HA solution, we focused our attention on the importance of persistent laminar flow conditions on inertio-elastic particle focusing. We first observed the flow behavior of 8-μm beads in HA for $Q < Q_t$. At Q = 0.6 ml.min^{-1} (Re = 105, Wi = 17), we observed particle migration towards a single centralized point along the channel centerline (Fig. 1C). This focusing behavior was also observed at flow rates as high as Q = 6 ml.min^{-1} (Fig. S9, Re = 1270, Wi = 170). The results obtained in the viscoelastic HA solution were in stark contrast to those in a Newtonian fluid. In water, beads initially focused to four off-center equilibrium positions near each face of the rectangular microchannel at Q = 0.6 ml.min^{-1} (Re = 140) before shifting to a five-point *quincunx* configuration at Q = 6 ml.min^{-1} (Re = 1400) with equilibrium positions at the centerline and the four channel corners, where the shear rate is lowest. These experimental

observations in water were in broad agreement with previous numerical studies of inertial migration in Newtonian fluids (*22*, *23*). Having established that particle focusing can be achieved for $Q < Q_t$ in both water and HA solution, albeit with significant configurational differences, we set $Q > Q_t$ to determine if deterministic particle focusing could be preserved in either fluid. For $Q > 13$ ml.min^{-1} in water ($Re > 2000$), particle tracking showed that the fluorescent beads were randomly distributed throughout the channel due to the onset of inertial turbulence, and this critical flow rate corresponded closely to the critical conditions beyond which ΔP_{water} increased superlinearly with increasing Q. Surprisingly, for $Q > Q_t$, beads in the HA solution continued to focus towards a centralized point along the channel centerline and we found that particle focusing in HA solution persisted to Reynolds numbers well above the upper limit for particle focusing in water. These results represent the highest flow rates at which deterministic particle focusing has been achieved in a microchannel, and illustrate the precise focusing control that can be achieved by using only small amounts of a viscoelastic drag-reducing polymeric agent (HA).

Given the well-known dependence of focusing efficiency on particle diameter a_p for inertial focusing (*24*, *25*), and creeping flows of viscoelastic fluids (*26*), we studied the effect of particle size on the inertio-elastic particle focusing observed in the HA solution. Using polystyrene beads with a_p = 1, 3, 6, or 8 μm, we found that particle focusing toward the channel center in HA solution improved with increasing particle size at $Q = 20$ ml.min^{-1} (Fig. 1D, $Re = 4422$, $Wi = 566$). Theoretical analysis of a single particle in the creeping flow limit (*27*) shows that the elastic lift force on a spherical particle in a weakly elastic fluid undergoing a pressure-driven shear flow scales as $F_{L,E} \sim \eta\lambda U^2(a_p/H)^3$. By contrast, the lateral resistive Stokes drag that resists

particle migration only scales linearly with particle size a_p and with the migration velocity u_{mig}. Hence, the value of u_{mig} is expected to scale strongly with a_p, meaning that a larger particle should require a much shorter distance to reach its equilibrium position. Using LEF images captured along the entire length of the microchannel at Q = 20 ml.min^{-1} (Fig. 1E), we found that 8-μm beads laterally migrated to their equilibrium position within an equilibrium focusing length $L_f \leq 30$ mm, based on the unchanged width of the focused streak further downstream. By contrast, at the same flow rate, lateral migration of 6-μm beads was incomplete within the channel length L = 35 mm.

In order to provide further insight into the physical basis of inertio-elastic particle focusing in the HA solution, we carried out a comparative study of water and HA solution within the laminar regime. For a given flow rate, we constructed vector plots of fluid velocity (Fig. 2A) based on 1-μm neutrally-buoyant beads being convected with the fluid through the microchannel, and also constructed "heat maps" of particle occurrence frequency across the channel cross-section based on the 2D position of 8-μm beads moving through the microchannel (Fig. 2B). We then combined the velocity profiles with the individual particle statistics (Fig. 2C). We first considered the effect of shear-thinning on particle focusing in HA solution. This was motivated by previous work (*11*) suggesting that shear-thinning in the fluid viscosity drives particles toward the wall. At Q = 0.09 ml.min^{-1}, we observed a markedly more blunt fluid velocity profile in the HA solution compared to water (Fig. 2C), which is consistent with shear-thinning behavior observed at $\dot{\gamma} \sim O(10^4)$ s^{-1} (Fig. S3) and with computational simulations using the Carreau model. At Q = 6 ml.min^{-1}, the characteristic shear rate in the fluid increased to $\dot{\gamma} \sim O(10^6)$ s^{-1} where the viscosity varied less strongly with shear rate. We continued to observe particle

focusing towards the center in the HA solution despite nearly identical fluid velocity profiles (measured using μ-PIV with 1-μm beads) for water and the HA solution (Fig. 2C). This result suggests that shear-thinning in the velocity profile did not play a dominant role in particle focusing under these flow conditions.

One important difference between the measured velocity profiles in water and the HA solution is the relationship between the average fluid velocity u_f and the corresponding particle velocity u_p once the focusing has fully developed (*i.e.*, $x > L_f$) (Fig. 2C). At each flow rate, the measured centerline velocity of the 8-μm beads in the HA solution was found to be faster than the local fluid velocity. For example, at $Q = 6.0$ ml.min^{-1} the measured velocity of the beads was $u_p = 30.9 \pm 0.7$ m.s^{-1} in the HA solution compared to a local fluid velocity of $u_f = 30.2$ m.s^{-1} (Fig. 2C). By contrast, in water, the particles along the centerline translated at $u_p = 28.2 \pm 0.9$ m.s^{-1}, which was slower than the local fluid velocity. These trends are consistent with (i) a drag *increase* expected for a sphere moving in a Newtonian channel flow, given by Faxén's law for creeping flow and an Oseen correction for fluid inertia (*28*, *29*), as well as (ii) the viscoelastic drag *decrease* on a sphere that is initially expected at a moderate particle Weissenberg number (*30*, *31*).

We also considered the effect of secondary flows on particle focusing in HA solution. This was motivated by recent work (*32*, *33*, *34*) showing that in channels with non-axisymmetric cross-section, normal stress differences in a viscoelastic fluid can drive secondary recirculating flows that are superposed on top of the primary axial flow field. Comparing the migration behavior of 8-μm beads in a 50-μm square (non-axisymmetric) channel and in a corresponding cylindrical

(axisymmetric) tube, we observed particle focusing toward the centerline in both cases. Gaussian fits to the LEF intensity profiles observed at $x > L_f$ were indistinguishable to within one particle diameter (Fig. S8), indicating that secondary flows did not play a significant role.

We then considered the effect of viscoelastic normal stress differences on particle focusing in HA solution. Early theoretical work in the creeping flow limit (*27*) has shown that particle migration in the direction of minimum shear rate (*i.e.*, towards the channel centerline) is induced by gradients in the normal stress differences that are present when the shear rate in the fluid varies laterally in the undisturbed flow field around the particle. Numerical simulations of particle sedimentation in quiescent viscoelastic fluids have also demonstrated that viscoelastic stresses drive particles towards the centerline of channels and tubes (*35*, *36*), and μ-PIV experiments have shown that fluid viscoelasticity can dramatically change the local velocity field around a particle near a wall (*37*). Fully developed numerical simulations of inertio-elastic particle migration are only just beginning to become feasible (and are presently limited to moderate Weissenberg numbers ($Wi < 50$) and Reynolds numbers ($Re < 40$) (*38*)) but having eliminated shear-thinning and secondary flows as primary drivers of this centerline focusing it is clear that the role of viscoelastic normal stresses cannot be neglected.

We used the deformability of human white blood cells (WBCs) to directly visualize the effects of normal stress differences in the fluid, which create an additional tensile stress along streamlines (14). Because of the high spatial fidelity and lack of particle blurring induced by the short duration of the pulsed laser imaging ($\delta t = 10$ ns), we are able to quantify the distortional effects of this streamline tension on the shape of an individual particle up to shear rates $\dot{\gamma} \sim O(10^6)$ s^{-1}.

The magnitude of WBC deformation was expressed in terms of a mean aspect ratio $AR = a_x/a_z$ (Fig. 3A). For WBCs suspended in PBS, the aspect ratio monotonically increased from $AR = 1.0$ (at $Q = 0.6$ ml.min^{-1}, $Re = 140$) to $AR = 1.2$ (at $Q = 13$ ml.min^{-1}, $Re = 3{,}033$) due to the increasing variation in the magnitude of the viscous shear stress acting across the WBC. By contrast, for WBCs suspended in the 1650 kDa HA solution, the aspect ratio monotonically increased from $AR = 1.4$ (at $Q = 0.6$ ml.min^{-1}, $Wi = 17$, $Re = 105$) to $AR = 2.5$ (at $Q = 13$ ml.min^{-1}, $Wi = 368$, $Re = 2{,}840$). However, we observed a breakdown in focusing of these deformable particles in both fluids at higher flow rates. For WBCs in a Newtonian fluid the focusing behavior was lost due to onset of turbulence for $Q > Q_t$. By contrast, the focusing capacity of WBCs in a viscoelastic fluid appeared to diminish due to a combination of excessive cell stretching and the corresponding reduction in the hydraulic diameter of the cells (Fig. 3B).

We have also investigated the role of fluid rheology in manipulating the interplay of particle focusing and particle stretching. In order to reduce the magnitude of the viscoelastic normal stresses experienced by WBCs, we used a lower molecular weight (357 kDa) HA solution. From the Zimm scaling for dilute polymer solutions ($\lambda \sim M_w^{0.8}$) we can estimate the relaxation time for this less viscoelastic solution to be $\lambda_{357\ \mathrm{kDa}} \approx 2.6 \times 10^{-4}$ s, and the Weissenberg number is reduced to $Wi \approx 100$ at $Q = 13$ ml.min^{-1}. Pulsed laser images indicate the maximum anisotropy in the cell dimensions was reduced to $AR = 1.4$ and we observed enhanced WBC focusing at flow rates beyond $Q = 13$ ml.min^{-1}. These results suggest that by tuning the nonlinear rheological properties of the viscoelastic working fluid it is possible to control both particle focusing and particle deformation.

Recent work (*39*, *40*) has suggested that inertial focusing of non-spherical particles depends on

the rotational diameter of a particle, regardless of its cross-sectional shape. Microscopic video imaging also shows that these particles rotate freely when suspended in a Newtonian fluid. To investigate the effect of particle shape on inertio-elastic focusing in HA solution at high Reynolds numbers, we used cylindrical cross-linked PEG particles synthesized via flow lithography (*41*). For a given PEG particle, we measured the lateral position z_p (with channel centerline defined by $z = 0$ μm) and the instantaneous orientation angle θ_p of the particle (with streamwise alignment defined by $\theta = 0°$) in the original HA solution at $Q = 20$ ml.min^{-1} (Fig. 3C). PEG particles in water occupied the entire range of lateral positions ($-40 \leq z \leq 40$ μm) and orientations ($-90° \leq \theta \leq 90°$). By contrast, in the HA solution, the PEG particles exhibited strong streamwise alignment along the channel centerline with $z_p \rightarrow 0$ and $\theta_p \rightarrow 0$. Similar streamwise alignment and migration to the centerline has been predicted in numerical simulations of the sedimentation of anisotropic particles in viscoelastic suspending fluids (*36*, *42*).

To summarize, we have demonstrated enhanced inertio-elastic focusing of rigid spherical beads, deformable WBCs, and anisotropic PEG particles using a common biopolymeric drag-reducing agent (HA) in a previously unexplored regime of Reynolds and Weissenberg numbers that can be accessed through the use of a rigid microfluidic device. We have demonstrated that there is a complex interaction between inertial effects in the flow and the viscoelastic fluid rheology that governs the migration, orientation and deformation of large (non-Brownian) particles suspended in the fluid. By varying the cross-sectional channel shape, the polymer molecular weight as well as the particle size and deformability, we have shown that it is not shear-thinning or the presence of secondary flows in the channel but elastic normal stresses in the fluid that drive the strong centerline focusing behavior observed. With sample processing rates of up to 3 L.hr^{-1} (and linear

velocities of 460 km.hr^{-1}) in a single microchannel, inertio-elastic particle focusing may ultimately be used for rapid isolation of tumor cells from large volumes of bodily fluid samples (*e.g.*, peritoneal washings, bronchoalveolar lavages, urine) (*43*), high-throughput intracellular delivery of macromolecules for therapeutic application (*44*), scanning of multifunctional encoded particles for rapid biomolecule analysis (*45*), and removal of floc aggregates within water treatment systems (*46*).

Acknowledgements:
We thank Bashar Hamza for his cell culture work, Bavand Keshavarz for rheological measurements of test fluids, and Patrick Nash for assembling the fluidic circuit. TJO acknowledges the NSF Graduate Research Fellowship for funding.

References and Notes:

1. R. D. Vidic, S. L. Brantley, J. M. Vandenbossche, D. Yoxtheimer, J. D. Abad, *Science*, **340**, 1235009 (2013).
2. M. A. Shannon *et al.*, *Nature*, **452**, 301 (2008).
3. S. Nagrath, L.V. Sequist *et al*., *Nature*, **450**, 1235 (2007).
4. L. R. Huang *et al.*, *Science*, **304**, 987 (2004).
5. W. R. Rodriguez *et al.*, *PLOS Med*., **2**, 0663 (2005).
6. D. Di Carlo, D. Irimia, R. G. Tompkins, M. Toner, *Proc. Natl. Acad. Sci. USA*, **104**, 18892 (2007).
7. J. Zhou, I. Papautsky, *Lab Chip*, **13**, 1121 (2013).
8. J. M. Martel, M. Toner, *Phys. Fluids*, **24**, 032001 (2012).
9. G. Guan *et al*., *Sci. Reports*, **3**, 1475 (2013).
10. A. T. Ciftlik, M. Ettori, M. A. M. Gijs, *Small*, **9**, 2764 (2013).
11. G. D'Avino *et al*., *Lab Chip*, **12**, 1638 (2012).
12. A. M., Leshansky, A. Bransky, A., N. Korin, U. Dinnar, *Phys. Rev. Lett.* **98**, 234501 (2007).
13. K. Kang, S. S. Lee, K. Hyun, S. J. Lee, J. M. Kim, *Nat. Commun*. **4**, 2567 doi: 10.1038/ncomms3567 (2013).
14. R. B. Bird, R. C. Armstrong, O. Hassager, *Dynamics of Polymeric Systems: Fluid Mechanics* (John-Wiley & Sons, 1987).
15. Crumeyrolle, O., Mutabazi, I., Grisel, M., *Phys. Fluids*, **14**, 1681 (2002).
16. M. D. Graham, *Phys. Rev. Lett.*, **89**, 208301 (2002).
17. E. J. Lim, T. J. Ober, J. F. Edd, G. H. McKinley, M. Toner, *Lab Chip*, **12**, 2199 (2012).
18. A. Cotoia, M. V. Kameneva, P. J. Marascalco, M. P. Fink, R. L. Delude, *Shock*, **31**, 258 (2009).

19. S. J. Haward, A. Jaishankar, M. S. N. Oliviera, M. A. Alves, G. H. McKinley, *Biomicrofluidics*, **7**, 044108 (2013).
20. Ardekani, A. M., Sharma, V., McKinley, G. H., *J. Fluid Mech.*, **665**, 46 (2010).
21. S. A. Vanapalli, S. L. Ceccio, M. J. Solomon, *Proc. Natl. Acad. Sci. USA*, **103**, 16660 (2006).
22. B. Chun, A. J. C. Ladd, *Phys. Fluids*, **16**, 031704 (2006).
23. D. Di Carlo, J. F. Edd, K. J. Humphry, H. A. Stone, M. Toner, *Phys. Rev. Lett.*, **102**, 094503 (2009).
24. D. Di Carlo, J. F. Edd, D. Irimia, R. G. Tompkins, M. Toner, *Anal. Chem.*, **80**, 2004 (2008).
25. S. S. Kuntaegowdanahalli, A. A. S. Bhagat, G. Kumar, I. Papautsky, *Lab Chip*, **9**, 2973 (2009).
26. S. Yang, J. Y. Kim, S. J. Lee, S. S. Lee, J. M. Kim, *Lab Chip*, **11**, 266 (2011).
27. B. P. Ho, L. G. Leal, *J. Fluid Mech.*, **76**, 783 (1976).
28. J. Happel, H. Brenner, *Low Reynolds number hydrodynamics: with special applications to particulate media* (Kluwer Boston Inc., 1983).
29. M. R. Maxey, J. J. Riley, *Phys. Fluids*, **26**, 883 (1983).
30. F. M. Leslie, R. I. Tanner, *Quart. J. Mech. Appl. Math.*, **14**, 36 (1961).
31. G. H. McKinley, *Steady and Transient Motion of a Sphere in an Elastic Fluid*, *Transport Processes in Bubbles*, *Drops & Particles*, Ch. 14 (Eds: R. Chhabra & D. DeKee) (Taylor & Francis, 2002).
32. S. C. Xue, N. Phan-Thien, R. I. Tanner, *J. Non-Newton. Fluid Mech.*, **59**, 191 (1995).
33. A. Zrehen, A. Ramachandran, *Phys. Rev. Lett.*, **110**, 018306 (2013).
34. M. M. Villone, G. D'Avino, M. A. Hulsen, E. F. Greco, P. L. Maffettone, *J. Non-Newton. Fluid Mech.*, **195**, 1 (2013).
35. P. Y. Huang, H. H. Hu, D. D. Joseph, *J. Fluid Mech.*, **362**, 297 (1998).
36. J. Hao, T. W. Pan, R. Glowinski, D. D. Joseph, *J. Non-Newton. Fluid Mech.*, **156**, 95 (2009).
37. J. A. Tatum, M. V. Finnis, N. J. Lawson, G. M. Harrison, *J. Non-Newton. Fluid Mech.*, **141**, 99 (2007).
38. M. R. Hashemi, R. Fatehi, M. T. Manzari, *J. Non-Newton. Fluid Mech.*, **166**, 1239 (2011).
39. S. C. Hur, S. E. Choi, S. Kwon, D. Di Carlo, *Appl. Phys. Lett.*, **99**, 044101 (2011).
40. M. Masaeli *et al*., *Phys. Rev. X*, **2**, 031017 (2012).
41. K. W. Bong *et al.*, *Nat. Commun.*, **3**, 805 (2012).
42. D. D. Joseph, Y. K. Liu, M. Poletto, J. Feng, *J. Non-Newton. Fluid Mech.*, **54**, 45 (1994).
43. E. Ozkumur, A. M. Shah *et al.*, *Sci. Transl. Med.*, **5**, 179ra147 (2013).
44. A. Sharei, J. Zoldan, A. Adamo *et al.*, *Proc. Natl. Acad. Sci. USA*, **110**, 2082 (2013).
45. D. C. Pregibon, M. Toner, P. S. Doyle, *Science*, **315**, 1393 (2007).
46. J. P. Wang, S. J. Yuan, Y. Wang, H. Q. Yu, *Water Res.*, **47**, 2643 (2013).
47. F. Durst, S. Ray, B. Unsal, O. A. Bayoumi, *J. Fluids Eng.*, **127**, 1154 (2005).
48. G. H. McKinley, A. Tripathi, *J. Rheol.*, **44**, 653 (2000).
49. F. M. White, *Fluid Mechanics* (McGraw-Hill, 2003).
50. B. P. Ho, L. G. Leal, *J. Fluid Mech.*, **65**, 365 (1974).
51. G. Segre, A. Silberberg, *Nature*, **189**, 209 (1961).

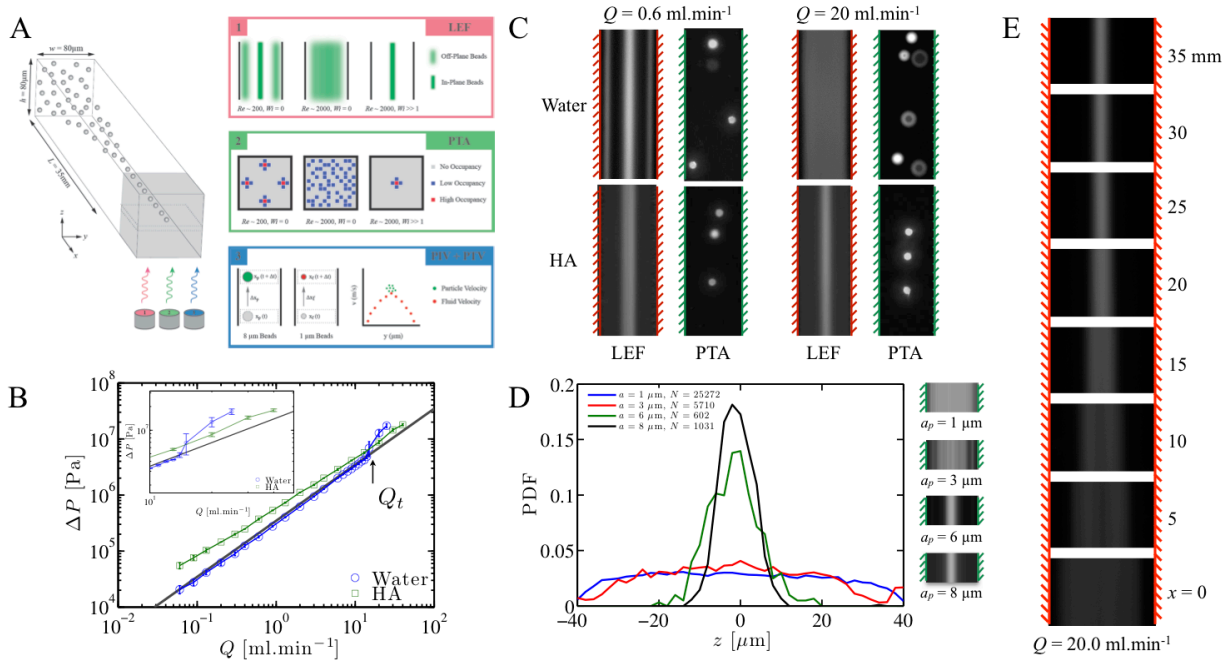

Figure 1. Particle migration in water breaks down under turbulent conditions at high flow rates but persists in HA solutions. (A) Imaging techniques used to observe 8-µm particles (particle velocity and position) and 1-µm particles (fluid velocity). (B) Pressure drop across the fluidic system. The solid gray line indicates the expected pressure drop for the laminar flow of water in the microchannel. Inset plot shows pressure drops near the onset of inertially turbulent flow at $Q = Q_t$. (C) LEF provides average particle distribution based on mean fluorescence intensity. PTA provides 2D particle histogram based on in-focus particles at a given imaging plane. The hashed lines indicate location of the rigid channel walls. A flow rate of Q = 0.6 ml.min^{-1} corresponds to Re = 140 in water, and to Re = 105 and Wi = 17 in the viscoelastic HA solution. A flow rate of Q = 20.0 ml.min^{-1}, corresponds to Re = 4360 in water, and Re = 4422 and Wi = 566 in HA. (D) Probability density function determined from N particles sized from a_p = 1, 3, 6 and 8 µm (volume fraction ϕ = 2.0% for 1 µm and ϕ = 0.05% for 3, 6 and 8 µm) across the channel width determined from short exposure images with pulsed laser illumination. The corresponding LEF images are shown adjacent to the plot. (E) LEF images of 8-µm particles at 5-mm intervals along the length of the channel at Q = 20 ml.min^{-1}, showing the lateral migration of the particles towards the centerline.

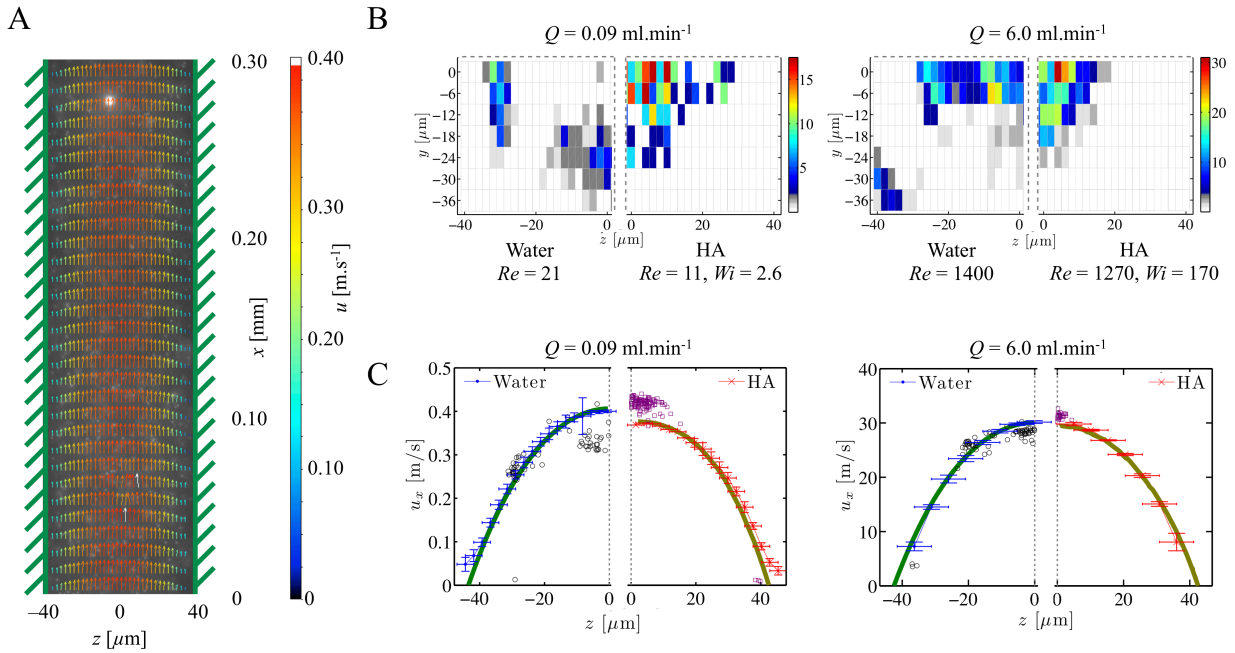

Figure 2. Potential mechanisms of inertio-elastic focusing are explored using individual particle statistics. (A) Representative fluid velocity field along the channel determined from a correlative μ-PIV technique. (B) Cross-sectional particle histogram of 8-μm particles in a lower quadrant of the square cross-section channel at Q = 0.09 ml.min^{-1} and at Q = 6.0 ml.min^{-1}. (C) Velocity profiles measured in the two fluids (red and blue curves respectively) and the corresponding velocities of the migrating 8-μm beads (black dots for beads in water and violet dots for beads in the HA solution) measured at the channel mid-plane (y = 0 μm). Note that at Q = 0.09 ml.min^{-1} in water, the particles occupy off-center equilibrium positions with four-fold symmetry. The particles that appear to be located at z = 0 in Fig 2C are projections of particles located around $y \approx \pm 25$ μm. For comparison, the expected velocity profiles at the mid-plane of the channel (*i.e.*, y = 0 μm) for the flow of a Newtonian fluid and a shear-thinning Carreau model (determined from COMSOL simulations) are shown by the green and gold curves, respectively.

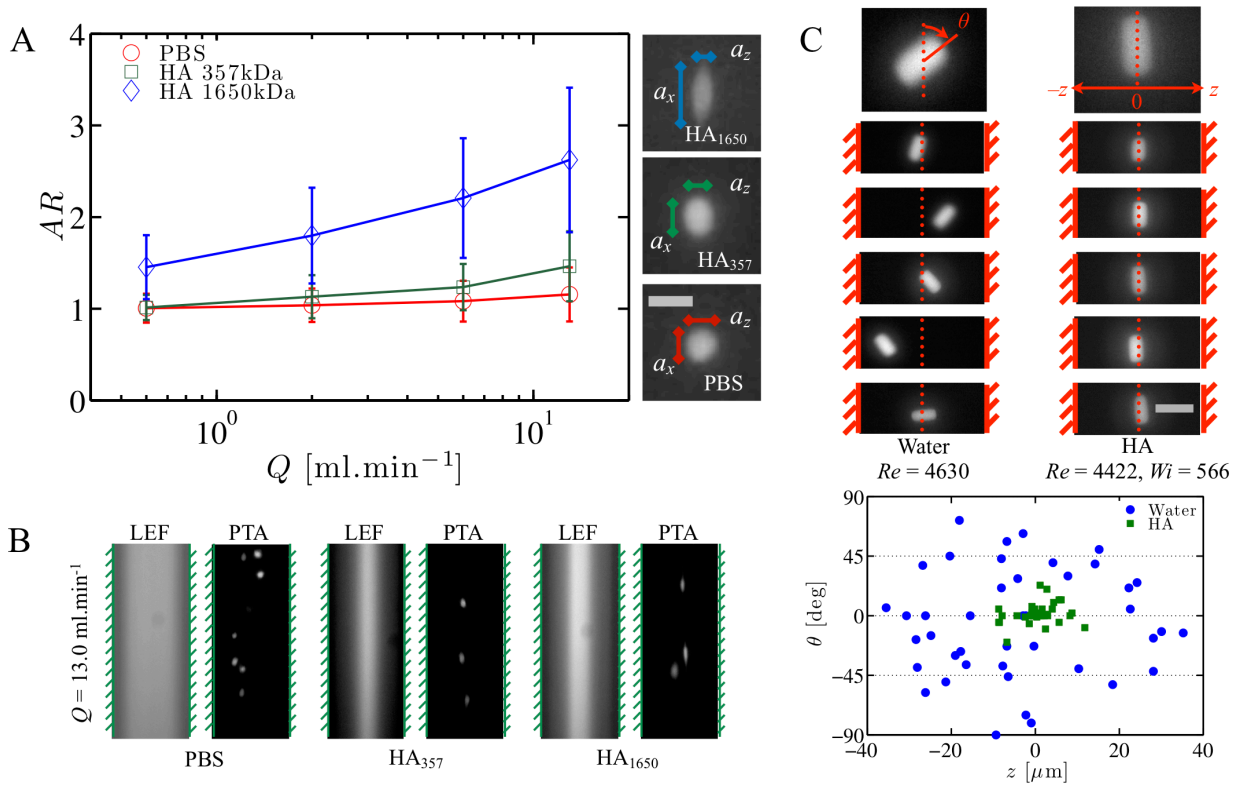

Figure 3. Inertio-elastic focusing of bioparticles based on deformability and shape. (A) Deformation statistics of WBCs in PBS, a low molecular weight (357 kDa) HA solution and a high molecular weight (1650 kDa) HA solution. The magnitude of WBC stretching is expressed in terms of aspect ratio $AR = a_x/a_z$. Scale bar equals 10 μm. (B) LEF and PTA images of WBCs in PBS, 357 kDa HA solution and 1650 kDa HA solution at $Q = 13$ ml.min^{-1}. (C) PTA images of PEG particles in 1650 kDa HA solution at $Q = 20$ ml.min^{-1}. Dashed red lines indicate channel centerline. Scale bar equals 30 μm. Measurements of lateral position z and instantaneous orientation angle θ are plotted for each PEG particle in water (blue) and in the HA solution (green).

Supplementary materials for:

Inertio-elastic focusing of bioparticles in microchannels at ultra-high throughput

Eugene J. Lim, Thomas J. Ober, Jon F. Edd, Douglas Neal, Ki Wan Bong, Patrick S. Doyle, Gareth H. McKinley & Mehmet Toner

Correspondence to: gareth@mit.edu, mehmet_toner@hms.harvard.edu

Section S1: Channel Fabrication and Design

For the construction of epoxy devices, channel features were created using computer-aided design software (AutoCAD) and printed on a Mylar mask (FineLine Imaging). SU-8 photoresist (MicroChem) was deposited onto a silicon wafer to produce a SU-8 master consisting of straight channels (L = 35 mm) with square (H = 80±5 μm) cross-section. Polydimethylsiloxane (PDMS) elastomer (Sylgard 184, Dow Corning) was poured over the SU-8 master to generate a PDMS replica (Fig. S1). The PDMS replica was peeled off and coated with (tridecafluoro-1,1,2,2-tetrahydrooctyl)trichlorosilane (Gelest) to produce a hydrophilic surface. PDMS elastomer was poured over the silane-coated PDMS replica to generate a hydrophobic PDMS master. The PDMS master was peeled off and punched with inlet and outlet holes using a coring tool (Harris Uni-Core). One end of a 7-mm strand of Teflon cord (McMaster-Carr) was partially inserted into a 13-inch strand of PEEK tubing (Sigma-Aldrich). The other end of the Teflon cord was partially inserted into the inlet and outlet holes of the PDMS master. Epoxy resin (EpoxAcast 690, Smooth-On) was poured over the PDMS master to generate an epoxy replica. After curing, the epoxy replica was separated from the flexible PDMS master, and the Teflon plugs were removed from the inlet and outlet holes. A 1-inch by 3-inch glass slide (Thermo Scientific) was coated with a 200-μm thick layer of epoxy resin. The epoxy replica and epoxy-coated glass slide were irreversibly bonded using mild (50°C) heat from a hot plate (Thermo Scientific) and gentle pressure using tweezers (Techni-Tool). For the construction of glass devices, borosilicate glass

tubing (VitroCom) with round (50-μm diameter) or square (50-μm height and width) cross-section was used. PEEK or Tygon tubing was bonded to a glass slide using an epoxy liquid (Loctite). Each end of the borosilicate glass tubing was inserted into PEEK or Tygon tubing using an epoxy gel (Loctite). The edges of the glass slide were covered with air-dry clay (Crayola), and the borosilicate glass tubing was submerged in an optically matched fluid (Sigma-Aldrich).

The height H and width W of the channel cross-section were chosen to maximize the Reynolds number for a given volumetric flow rate Q and hydraulic diameter $D = 2HW/(H+W)$. The channel Reynolds number Re_c can be expressed as

$$Re_c = \frac{QD}{HW\nu} = \frac{4Q}{D\nu}\frac{\alpha}{(1+\alpha)^2}$$

where ν is the kinematic viscosity of the fluid and $\alpha = H/W$ is the aspect ratio (with the constraint that $0 \leq \alpha \leq 1$). For a constant ratio of Q/D, the value of Re_c is maximized when $\alpha = 1$ (Fig. S2). The length L of the channel was chosen to ensure that the flow was hydrodynamically fully-developed for all Re_c over which the flow was laminar. For the flow of a Newtonian fluid in a rectilinear duct (*47*), the hydrodynamic entrance length L_e can be expressed as

$$L_e = D\left[0.619^{1.6} + \left(0.0567Re_c\right)^{1.6}\right]^{\frac{1}{1.6}}$$

with the additional condition that $L_e < L < L_s$, where L_s is the length of the epoxy-coated glass slide. The transition to inertially-dominated turbulence is expected to occur at $Re_c \sim 2000$, which suggests that $L_e = 113D$. For polystyrene beads with particle diameter $a = 8$ μm, we set the hydraulic diameter $D = W = H = 80$ μm such that the ratio of particle diameter to channel dimension $a/D \geq 0.1$. This ensured that the particle Reynolds number is $Re_p \sim O(1)$ for

Re_c < 2000. For a straight channel with 80-μm square cross-section, we set the channel length L = 3.50 mm, which significantly exceeded the entrance length L_e = 0.90 mm for Re_c ~ 2000.

Section S2: Sample Preparation

Hyaluronic acid (HA) sodium salt (Sigma-Aldrich or Lifecore Biomedical) was added to water (Sigma-Aldrich) for bead suspensions or phosphate buffered saline (PBS) solution (Life Technologies) solution for cell suspensions and prepared using a roller mixer (Stuart, Sigma-Aldrich). Polystyrene beads (FluoSpheres, Invitrogen or Fluoro-Max, Thermo Scientific) suspended in Tween-20 (Sigma-Aldrich) solution (0.1% v/v, water) were diluted in HA solution (1650 kDa, 0.1% w/v, c/c^* = 10 (*19*), water) at a concentration of 3 x 10^6 beads.ml^{-1}. Human leukemia cell lines (HL-60, ATCC) were suspended in Iscove's Modified Dulbecco's Medium (ATCC) containing 20% FBS (Gibco) and incubated at 37°C and 5% CO_2. HL-60 cells were centrifuged and suspended in Calcein Red-Orange (Invitrogen) solution (2 μg.ml^{-1}, PBS). Fluorescently labeled HL-60 cells were centrifuged and suspended in PBS or HA solution (1650 kDa, 0.1% w/v, PBS) at a concentration of 1 x 10^6 cells.ml^{-1}. White blood cells (WBCs) were harvested from human Buffy coat samples (MGH Blood Bank) via density gradient centrifugation (Histopaque-1077, Sigma-Aldrich). WBCs were centrifuged and suspended in Calcein Red-Orange solution (10 μg.ml^{-1}, PBS). Fluorescently labeled WBCs were centrifuged and suspended in PBS, low molecular weight HA solution (357 kDa, 0.1% w/v, PBS) or high molecular weight HA solution (1650 kDa, 0.1% w/v, PBS) at a concentration of 5 x 10^6 cells.ml^{-1}. Anisotropic (cylindrical) hydrogel particles were synthesized via stop-flow lithography (*41*) from pre-polymer solutions of 60% poly(ethylene glycol) diacrylate (PEG-DA 700, Sigma-Aldrich), 30% poly(ethylene glycol) (PEG 200, Sigma-Aldrich), 10% 2-hydroxy-2-

methylpropiophenon (Sigma-Aldrich), and 3 mg.ml^{-1} rhodamine acrylate (Polysciences). Fluorescently labeled PEG particles (20-μm length, 10-μm cross-sectional diameter) were collected and washed in Tween-20 solution (0.1% v/v, PBS) prior to dilution in HA solution (1650 kDa, 0.1% w/v, water).

The viscosity of all fluid samples was measured using both a stress-controlled rheometer (DHR-3, TA Instruments) and a microfluidic viscometer-rheometer-on-a-chip (VROC, Rheosense) (Fig. S3). The DHR-3 instrument imposed an increasing shear rate ramp on a fluid sample contained within a double-gap cylindrical Couette cell. The viscosity of the fluid sample was measured on the DHR-3 instrument for shear rates $0.1 < \dot{\gamma} < 3 \times 10^3$ s^{-1}. The VROC microfluidic chip consists of a borosilicate glass microchannel with a rectangular slit cross-section and a silicon pressure sensor array. The viscosity of the fluid sample was measured on the VROC device for shear rates $5 \times 10^3 < \dot{\gamma} < 3.3 \times 10^5$ s^{-1}. In order to numerically predict the velocity profiles in the channel, the measured flow curve of the native sample was fit with the Carreau model

$$\eta(\dot{\gamma}) = \eta_\infty - (\eta_0 - \eta_\infty)\left[1 + (\dot{\gamma}/\dot{\gamma}^*)^2\right]^{\frac{n-1}{2}}$$

where η_∞ is the infinite-shear-rate viscosity, η_0 is the zero-shear-rate viscosity, $\dot{\gamma}^*$ is a characteristic shear rate at the onset of shear-thinning, and *n* is the ‘‘power-law exponent’’.

We measured the fluid viscosity of both native and used samples of HA solution at $Q = 20$ ml.min^{-1} to investigate the role of shear-induced sample degradation. The viscosity of native HA solution exceeded the viscosity of used HA solution by at least a factor of 2 for shear rates $0.1 <$

$\dot{\gamma} < 10^3$ s^{-1} presumably due to the shear-induced disruption of aggregates in the solution. However, the measured difference in HA viscosity between the samples was minimal and remained unchanged after repeated shearing for the high shear rates ($10^3 < \dot{\gamma} < 10^7$ s^{-1}) explored in this study. This suggests that irreversible polymer degradation had little to no effect on HA viscosity at the flow rates where particle focusing was observed.

The relaxation time λ of the native HA solution was measured based on thinning dynamics in jetting experiments (*20*). As a viscoelastic liquid bridge thins, the diameter of the filament D will decay according to the relation (*48*)

$$\frac{D}{D_0} \propto e^{-t/3\lambda}$$

where D_o is the initial diameter of the filament. When plotted on semi-logarithmic axes, the initial slope of filament decay is equal to -1/3λ (Fig. S4).

Section S3: Pressure Drop Measurements

Fluid flow through the microchannel was achieved using a syringe pump (100DX, Teledyne Isco) capable of a maximum volumetric flow rate of 50 $ml.min^{-1}$, a maximum pressure of 10000 PSI, and a maximum capacity of 103 ml. A stainless steel ferrule adapter (Swagelok) connected the syringe pump to the PEEK tubing embedded in the epoxy chip. The syringe pump's internal pressure transducer was used to obtain pressure drop measurements across the entire fluidic circuit. However, we found that the hydrodynamic resistance of the microchannel accounted for approximately 99% of the overall hydrodynamic resistance. As a result, we considered the pressure drop measured by the syringe pump to be essentially equal to the pressure drop along

the microchannel. The pressure drop ΔP was an essential parameter in determining the Fanning friction factor f, defined for laminar flow of a Newtonian fluid through a square microchannel as

$$f = \frac{\Delta P}{0.5\rho U^2 (L/D)} = \frac{96}{(1+\alpha)^2}\left[1 - \frac{192}{\pi^5}\alpha \sum_{j=odd}^{\infty} \frac{\tanh(j\pi/2\alpha)}{j^5}\right]^{-1} \frac{1}{Re_c} = \frac{56.9}{Re_c}$$

where U is the mean fluid velocity in the channel, L is the channel length, D is the channel hydraulic diameter, and Re_c is the channel Reynolds number. In this operating regime, ΔP increased linearly with Q, and f scaled inversely with Re_c. For $Re_c > 2000$ (where the channel flow is expected to be turbulent), f can be expressed in a microchannel (*49*) as

$$f = \left[-1.8 \ln\left(\frac{6.9}{Re_c}\right) + \left(\frac{\varepsilon}{3.7}\right)^{1.11}\right]^{-2}$$

where $\varepsilon = k/D$ is the ratio of the average surface roughness on the channel wall k to the channel hydraulic diameter D. The typical surface roughness was $k \sim O(1\ \mu m)$ for the epoxy channels used in this study. As a conservative estimate, we set $\varepsilon \sim 0.01$ to calculate f as a function of Re_c. The characteristic viscosity was an essential parameter for determining the channel Reynolds number, and the Carreau model was used to calculate the characteristic viscosity as a function of wall shear rate. For Newtonian flow in a square microchannel (*i.e.*, $\alpha = 1$), the analytical solution (*48*) of wall shear rate $\dot{\gamma}_{w,3D}$ can be expressed as

$$\dot{\gamma}_{w,3D} = \frac{U}{D}\frac{96}{\pi^2(1+\alpha)}\left[\sum_{j=odd}^{\infty} \frac{1 - \frac{1}{\cosh(j\pi/2\alpha)}}{j^2}\right]\left[1 - \frac{192}{\pi^5}\alpha \sum_{j=odd}^{\infty} \frac{\tanh(j\pi/2\alpha)}{j^5}\right]^{-1} = 9.4\frac{U}{D}$$

When the characteristic viscosity (based on wall shear rate) is used to calculate Re_c, the friction factor of the HA solution f_{HA} collapses onto the expected curve for a Newtonian fluid (Fig. S5).

Section S4: Velocimetry Measurements

Images of fluorescent particles in the microchannel were acquired with a double-pulsed 532-nm Nd:YAG laser (LaVision), a 1.4-megapixel CCD camera (PIV-Cam 14-10, TSI), and an epifluorescence microscope (TE-2000, Nikon). Particle velocity measurements were made with 8-μm polystyrene beads (3 x 10^6 beads.ml^{-1} water or HA solution), and fluid velocity measurements were made with 1-μm polystyrene beads (3 x 10^8 beads.ml^{-1} water or HA solution). For a given pair of laser pulses, the duration of a single pulse was δt = 10 ns, and the time interval between the two pulses was user-defined depending on the speed of the flow being imaged. At a given *x*-*z* plane, particle tracking velocimetry (PTV) was used to record the displacement of 8-μm beads in the *x*-direction over a given time interval (Fig. S6). PTV images were processed in MATLAB (MathWorks) to generate a set of individual particle velocity measurements. At the same *x*-*z* plane, micro particle image velocimetry (μ-PIV) was used to record the displacement of 1-μm beads within an array of interrogation windows over a given time interval. For $Q < 0.1$ ml.min^{-1}, the particle displacement $2a_p < \Delta x < 7.5a_p$ was sufficiently low to enable image analysis using a cross-correlation μ-PIV algorithm (TSI). For $Q > 0.1$ ml.min^{-1}, it became necessary to acquire single images that were double-exposed, and these images were analyzed using an auto-correlation μ-PIV algorithm (LaVision).

Section S5: Lateral Particle Migration and Equilibrium Position

We estimated the lateral particle migration based on the change in the full width at half max (FWHM) of the LEF images captured at Δx = 5-mm intervals along the channel length at Q = 0.6, 6.0 and 20 ml.min^{-1}. The migration velocity is approximately given by $u_{mig} \approx \Delta(\text{FWHM})/2\Delta t$, where $\Delta t = \Delta x/U$ and the factor of two in the denominator results from the fact

that particles migrate towards the channel centerline from both sides of the channel. The values of u_{mig} decreased along the channel length (Fig. S7a) as the particles asymptotically approach the channel centerline $(y,z) = (0,0)$. The ratio of u_{mig}/U also increased with Q, indicating that at higher Q the particles can reach their equilibrium position using a shorter channel length.

Inertial migration in a Newtonian liquid in two-dimensional Poiseuille flow has been treated analytically (*50*) using the method of reflections. The inertial lift force at the position z in the channel is given by the equation

$$F_L^I = \frac{81}{8}\left(\frac{a_p}{H}\right)^4 \rho U^2 H^2 \left\{\frac{z}{H}\left[2\frac{z}{H}G_1\left(\frac{z}{H}\right) - G_2\left(\frac{z}{H}\right)\right]\right\}$$

where G_1 and G_2 are functions of z/H that are determined using the Lorentz reciprocal theorem and must be evaluated numerically to solve for the resulting lift force. When the net inertial lift force on the particle is zero, the particle equilibrates to a position $z_{eq}/H = 0.3$, which is similar to the dimensionless radial equilibrium position for flow in a pipe found experimentally (*51*).

Elastic migration in a second order fluid has been studied analytically (*27*), and the viscoelastic lift force on a particle is given by

$$F_L^{VE} = -15\pi \frac{a_p^3}{H}\left(\frac{z}{H}\right)\left(\Psi_1 - 2\Psi_2\right)\left(\frac{U}{H}\right)^2$$

where Ψ_1 and Ψ_2 are the first and second normal stress coefficients of the fluid, respectively. For most viscoelastic liquids $\Psi_1 > -\Psi_2 > 0$, hence the viscoelastic lift force tends to drive a particle towards the channel centerline (*i.e.*, $z_{eq} = 0$). We simplified this equation by setting $\Psi_1 \sim \eta\lambda$ and $\Psi_2 = 0$ in the main text.

Considerable insight can be gained from these equations to determine the competing effects of inertia and viscoelasticity acting simultaneously on the particle equilibrium position. Equating the two forces to determine the equilibrium position of the particle across the channel width, one obtains the implicit equation

$$2\frac{z_{eq}}{H}G_1\left(\frac{z_{eq}}{H}\right)-G_2\left(\frac{z_{eq}}{H}\right)=\frac{40\pi}{27}\frac{\Psi_1-2\Psi_2}{\rho a_p H}$$

The dimensionless parameter on the right hand side of this equation is a hybrid *elasticity number* that depends on both the channel dimension H and the particle diameter a_p. For values of the elasticity number much less than one, inertia dominates and there are multiple equilibrium positions, whereas particles equilibrate along the channel centerline as the elasticity number is increased above $O(1)$ (Fig. S7b).

Section S6: Secondary Flow Effects

For microchannels with non-axisymmetric cross-section, normal stress differences in a viscoelastic fluid can drive secondary recirculating flows (*32*, *33*, *34*). To observe the effect of secondary flows on particle migration in a viscoelastic fluid, we used borosilicate glass microchannels with round (axisymmetric) or square (non-axisymmetric) cross-section. Particle distributions of 8-μm polystyrene beads in HA solution were obtained using PTA for both microchannels (Fig. S8). For a range of Re_c corresponding to those studied in the epoxy microchannels, particle focusing toward the channel centerline was observed in both axi-symmetric and non-axisymmetric microchannels. At x = 35 mm (which was beyond the equilibrium focusing length L_f), Gaussian fits to the LEF intensity profiles were indistinguishable to within one particle diameter, indicating that secondary flows did not play a significant role.

Section S7: Effects of Viscoelastic Normal Stress Differences

For Q = 6 ml.min^{-1}, we observed one common equilibrium focusing position at the channel centerline for 8-μm polystyrene beads in water and HA solution (Fig. S9). In order to characterize the importance of normal stress differences in the HA solution, we had to find a particle whose response to these effects could be visualized in some manner. We selected HL-60 cells based on their sphericity and deformability, and we fluorescently labeled these cells with Calcein Red-Orange. We observed the shape of individual HL-60 cells occupying the common equilibrium position in the channel center using PTA (Fig. S10). The magnitude of cell stretching was calculated based on the ratio of maximum cell diameter measured along the x-axis to maximum cell diameter measured along the z-axis. For Q = 6 ml.min^{-1}, we observed a mean aspect ratio of 1.4 for HL-60 cells in PBS and 2.8 for HL-60 cells in HA solution. For Q = 13 ml.min^{-1}, single-stream focusing of HL-60 cells was not observed for the two fluids tested, but the limiting factor was different in each case. For HL-60 cells in PBS, the focusing behavior was lost due to onset of turbulence. By contrast, the focusing capacity of HL-60 cells in HA solution appeared to diminish due to a combination of excessive cell stretching and the corresponding reduction in hydraulic diameter of the cells. These results suggest that viscoelastic normal stresses play a critical role in both particle focusing and particle stretching as it relates to deformable particles.

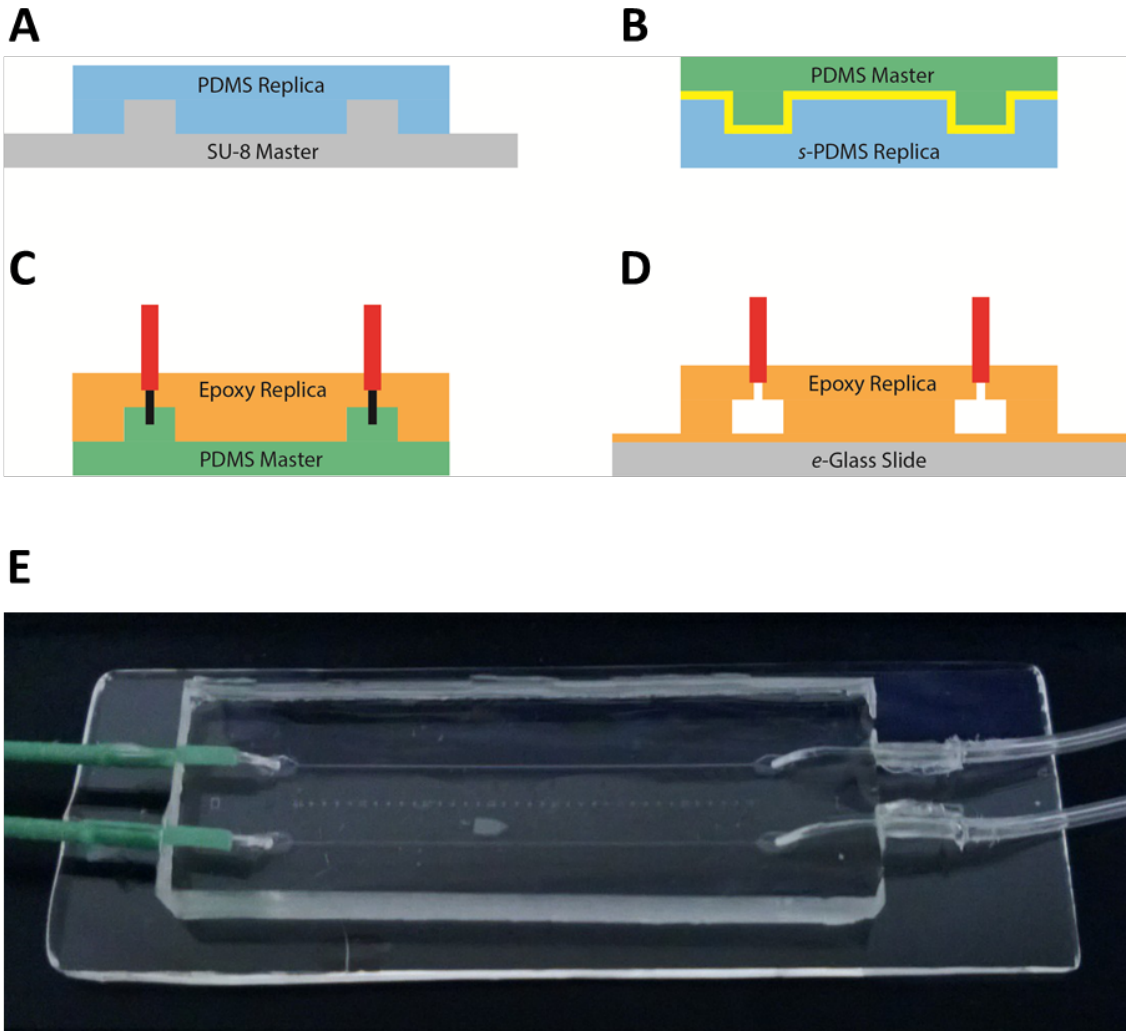

Figure S1. Fabrication of epoxy microchannels. **(A)** PDMS replica is generated from SU-8 master via soft lithography. **(B)** PDMS master is peeled away from PDMS replica and treated via vapor deposition with (tridecafluoro-1,1,2,2-tetrahydroocttyl)trichlorosilane. **(C)** Epoxy replica is generated from the PDMS master and fitted with Teflon plugs (black) and PEEK or Tygon tubing (red). **(D)** Epoxy replica (with Teflon plugs removed) is bonded to epoxy-coated glass slide. **(E)** Bright-field image of 35-mm long straight channel with 80-µm square cross-section. PEEK tubing is connected to the channel inlet (high-pressure end), and Tygon tubing is connected to the channel outlet (low-pressure end).

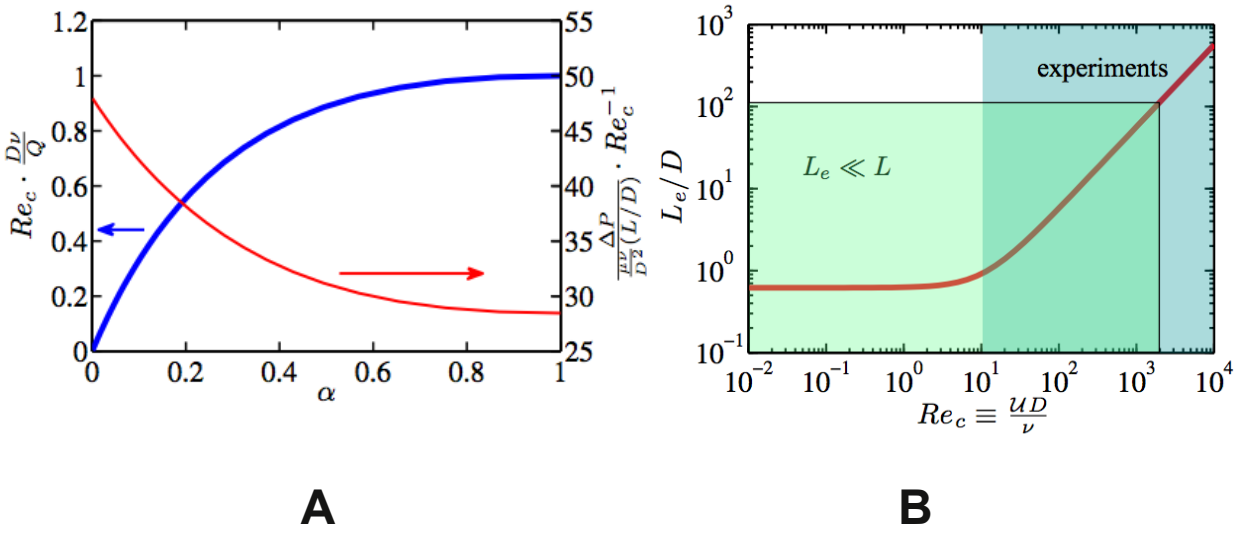

Figure S2. Design parameters for microchannel dimensions. **(A)** Plot of channel Reynolds number normalized for a constant ratio of Q/D, and friction factor normalized for a constant value of Re_c as a function of channel aspect ratio $\alpha = W/H$. **(B)** Hydrodynamic entrance length as a function of channel Reynolds number.

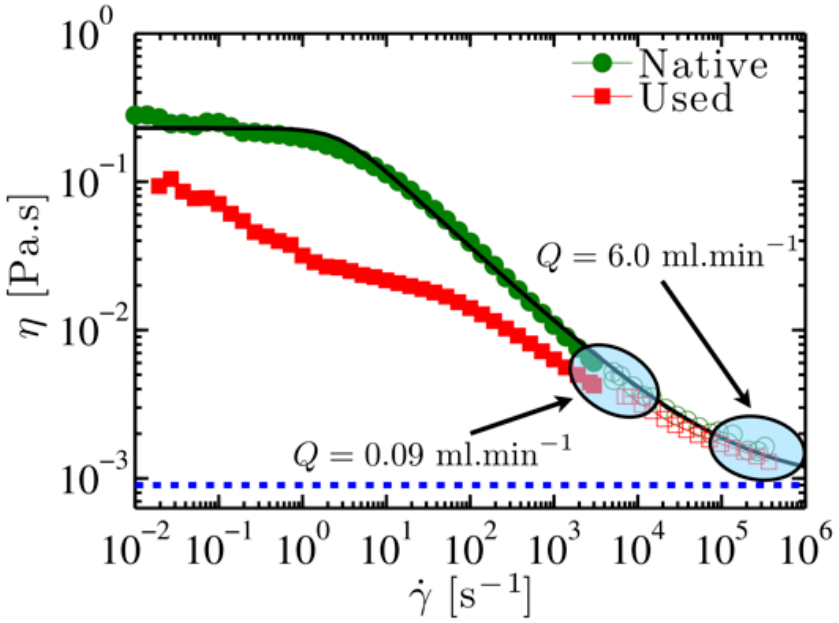

Figure S3. Rheological measurements of HA solutions. Flow curve of HA solution before use ("native") and after use ("used") at flow rates up to $Q = 20$ ml.min^{-1}. Carreau model fit to unused HA solution, $\eta_0 = 230$ mPa.s, $\eta_\infty = 0.9$ mPa.s, $\dot{\gamma} = 0.36$ s^{-1}, $n = 0.48$. Water viscosity ($\mu_w = 0.9$ mPa.s) is shown by blue dashed line.

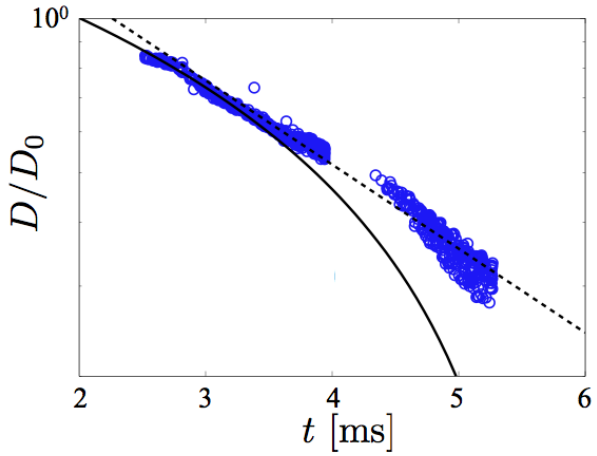

Figure S4. Relaxation time measurement of HA solution. Diameter $D(t)$ of a thinning HA (M_w = 1650 kDa) filament bridge as a function of time t. The dashed line in the figure indicates the initial slope from jetting experiments used to calculate the effective relaxation time. The solid line indicates the visco-capillary break up profile of a Newtonian liquid. The relaxation time was determined to be $\lambda = 8.7 \times 10^{-4}$ s.

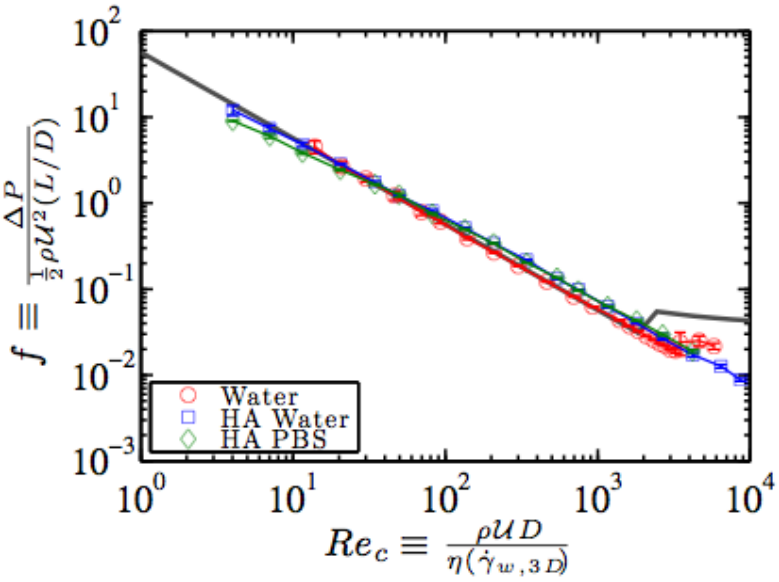

Figure S5. Fanning friction factor in microchannel for Newtonian and viscoelastic fluids. Fanning friction factor f as a function of channel Reynolds number Re_c based on a shear rate-dependent viscosity evaluated at the characteristic shear rate at the wall of a microchannel with square cross-section. The gray line indicates the theoretical friction factor for a Newtonian fluid.

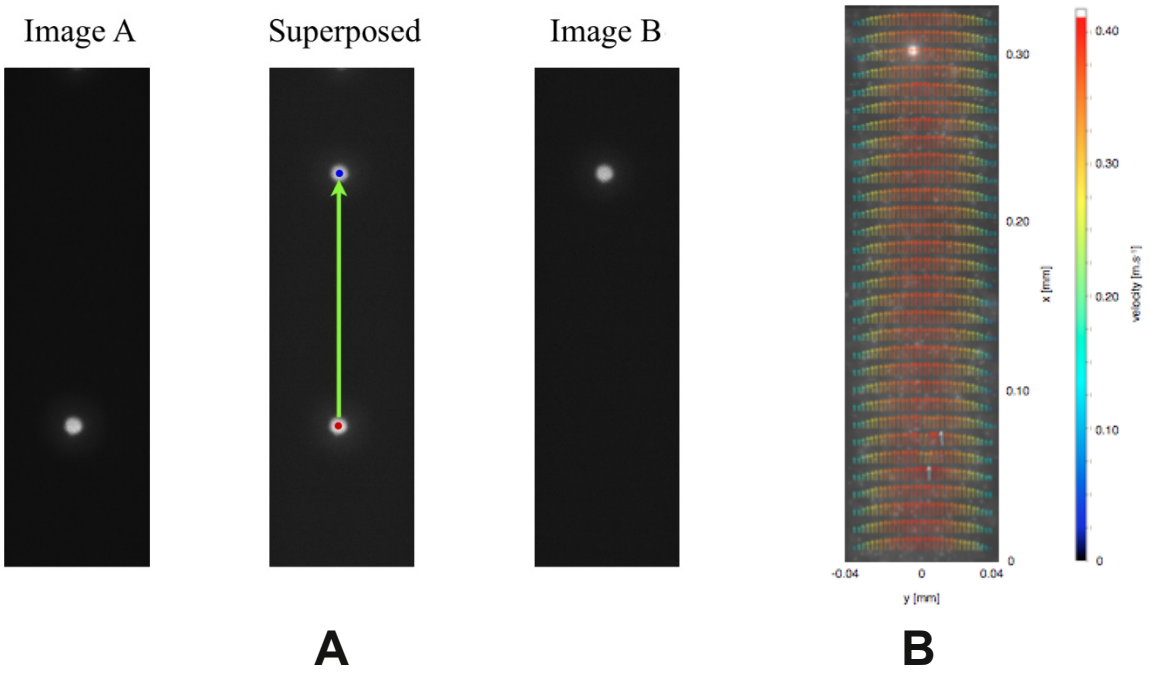

Figure S6. Velocimetry measurements of polystyrene beads in Newtonian and viscoelastic fluids. **(A)** Representative particle tracking velocimetry (PTV) image pair for determining the velocity of individual 8-µm beads in the microchannel. The exposure time of each frame is δt = 10 ns, and the time interval between Image A and Image B is Δt = 50 µs. **(B)** Representative full-field map of the fluid velocity profile in the microchannel determined from correlative micro particle image velocimetry (µ-PIV) analysis of individual 1-µm beads seeded throughout the fluid sample.

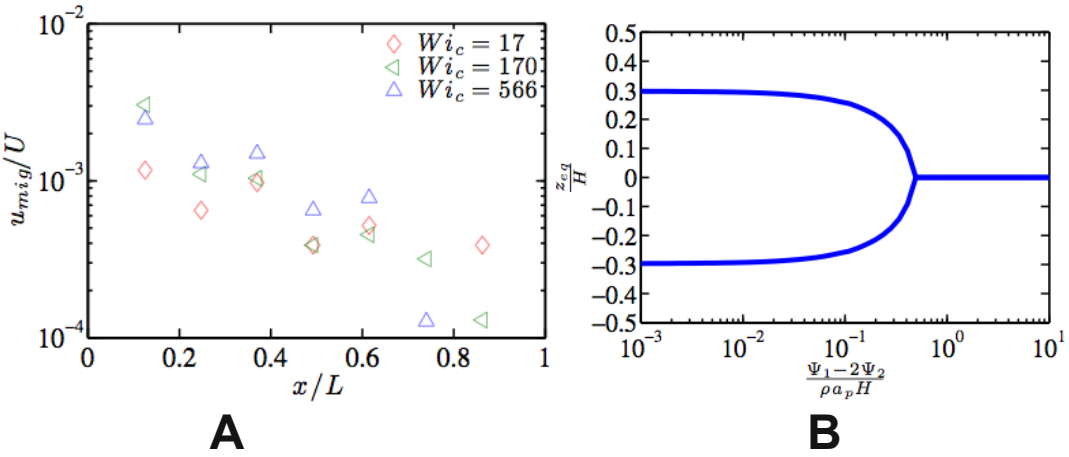

Figure S7. Particle migration dynamics in HA solution. (**A**) Elastically dominated lateral migration velocity of 8-µm particles along the channel length at Q = 0.6, 6 and 20 ml.min^{-1} (U = 1.6, 16 and 52 m.s^{-1}). (**B**) Dimensionless particle equilibrium position z_{eq}/H as a function of the hybrid elasticity number, calculated using creeping flow theory. The equilibrium migration behavior is increasingly dominated by elasticity for particles of smaller diameter a_p.

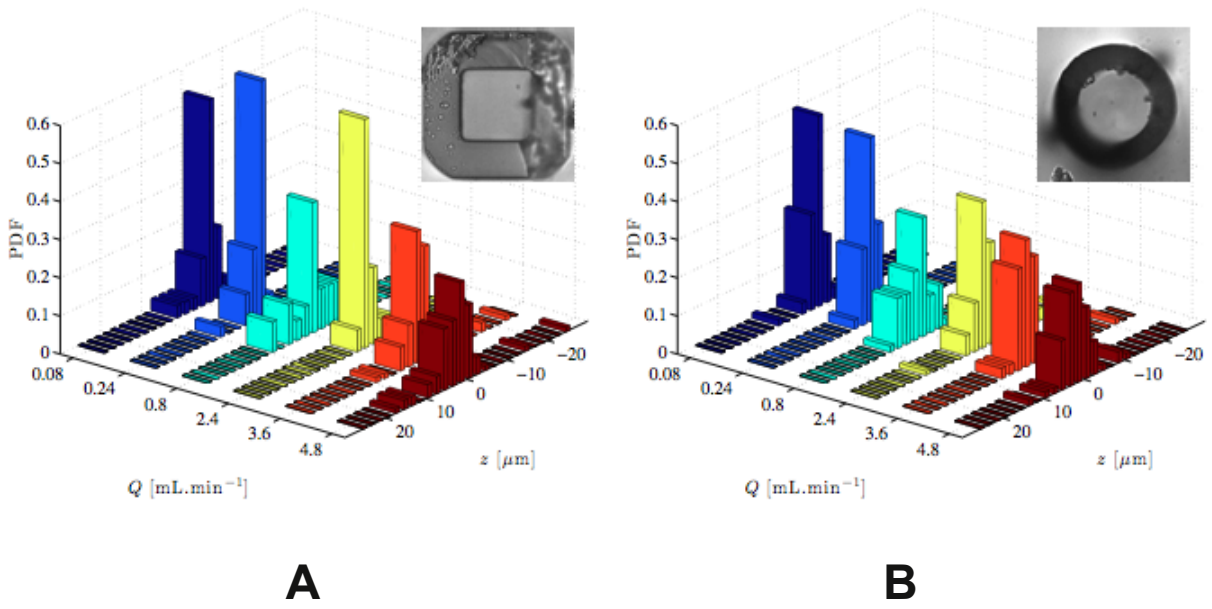

Figure S8. Secondary flow effects in HA solution. Particle distributions across the channel width over a range of flow rates in; **(A)** a borosilicate glass microchannel with square (inner dimension = 50 μm) cross-section, and **(B)** a borosilicate glass microchannel with cylindrical (inner diameter = 50 μm) cross-section. Inset figures show bright-field images of the borosilicate glass microchannels.

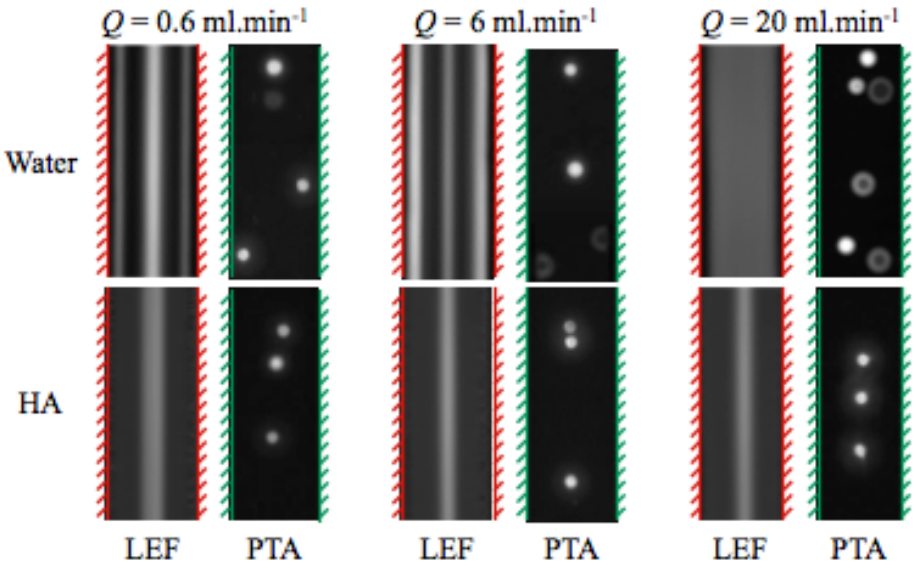

Figure S9. Particle migration behavior in water and HA solution. Long-exposure fluorescence (LEF) characterizes particle focusing behavior based on aggregate signal intensity of particle populations. Particle trajectory analysis (PTA) characterizes particle focusing behavior based on individual particle statistics. The hashed lines indicate the position of the channel walls. At Q = 0.6 ml.min^{-1}, Re = 140 in water, and Re = 105 and Wi = 17 in HA. At Q = 6.0 ml.min^{-1}, Re = 1400 in water, and Re = 1270 and Wi = 170 in HA. At Q = 20.0 ml.min^{-1}, Re = 4360 in water, and Re = 4422 and Wi = 566 in HA.

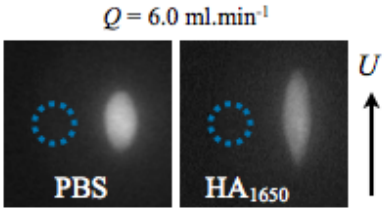

Figure S10. Visualization of viscoelastic normal stress differences. Deformation of HL-60 cells along the channel centerline in PBS and HA solution at Q = 6.0 ml.min^{-1}. The dotted blue circle represents an undeformed sphere with diameter a_p = 12 μm.